




## Larger wavelengths suit hydrodynamics of carangiform swimmers

Muhammad Saif Ullah Khalid <sup>1,2,3</sup>, Junshi Wang <sup>4</sup>, Imran Akhtar,<sup>5</sup> Haibo Dong,<sup>4</sup>  
Moubin Liu,<sup>1,2,\*</sup> and Arman Hemmati <sup>3</sup>

<sup>1</sup>Key State Laboratory of Turbulence and Complex Flows, Department of Mechanics, Peking University, Beijing 100871, People's Republic of China

<sup>2</sup>Institute of Ocean Research, Peking University, Beijing 100871, People's Republic of China

<sup>3</sup>Department of Mechanical Engineering, University of Alberta, Edmonton, T6G 1H9 Alberta, Canada

<sup>4</sup>Department of Mechanical and Aerospace Engineering, University of Virginia, Charlottesville, Virginia 22904, USA

<sup>5</sup>Department of Mechanical Engineering, NUST College of Electrical & Mechanical Engineering, National University of Sciences & Technology, Rawalpindi 46000, Pakistan



(Received 19 January 2021; accepted 3 June 2021; published 9 July 2021)

The wavelength of undulatory kinematics of fish is an important parameter to determine their hydrodynamic performance. This study focuses on numerical examination of this feature by reconstructing the real physiological model and kinematics of steadily swimming Jack Fish. We perform three-dimensional numerical simulations for flows over these models composed of the trunk, and dorsal, anal, and caudal fins. Moreover, we prescribe the carangiform-like motion for its undulation for a range of wavelengths. Undulation with larger wavelengths improves the hydrodynamic performance of the carangiform swimmer in terms of better thrust production by the caudal fin, lower drag production on the trunk, and reduced power consumption by the trunk. This coincides with the formation of stronger posterior body vortices and leading-edge vortices with more circulation on the caudal fin. The real kinematics of Jack Fish surpasses the performance of those with prescribed motion owing to the flexibility of the caudal fin.

DOI: [10.1103/PhysRevFluids.6.073101](https://doi.org/10.1103/PhysRevFluids.6.073101)

### I. INTRODUCTION

Due to limited capabilities of torpedo-shaped autonomous underwater vehicles in comparison to natural aquatic species [1], extensive research currently focuses on understanding the kinematics and hydrodynamic mechanisms employed by fish to efficiently perform various swimming maneuvers [2–9]. Understanding these natural functions helps us tremendously to develop better bio-inspired robotic systems capable of handling extreme environments in large water reservoirs, such as oceans and rivers. In this context, a wide range of prospective applications in both civil and military domains makes it more attractive to further develop our knowledge of the fish swimming mechanics.

Considering their gaits and kinematics, fish are classified on the basis of the wavelength ( $\lambda$ ) with which they undulate their bodies for propulsion. Most commonly known classes are anguilliform, subcarangiform, carangiform, and thunniform. As explained by Sfakiotakis *et al.* [10] and Lauder and Madden [11], anguilliform swimmers undulate their bodies at wavelengths ( $\lambda$ ) shorter than their body lengths ( $L$ ), that is,  $\lambda \ll L$ . In the case of subcarangiform and carangiform,  $\lambda$  is observed to be either equal to or slightly larger than  $L$ , i.e.,  $\lambda/L \approx 1$ . Thunniform swimmers primarily employ their caudal fins with almost no oscillations of their trunks and  $\lambda/L \gg 1$ .

\*Corresponding author: [mbliu@pku.edu.cn](mailto:mbliu@pku.edu.cn)

Bio-inspired underwater robots can be designed using the fish physiology and kinematics to match their hydrodynamic performance [1,2,7]. To this end, it becomes imperative to investigate the link between fish morphological structures and their gaits.

Carangiform swimmers have remained mostly popular in the scientific community perhaps due to their efficiency and swimming speed. In recent years, many research efforts have been directed towards elucidating the hydrodynamics of this class of fish [12–17]. Initially, Müller *et al.* [18] have used two-dimensional (2D) particle image velocimetry to determine that a swimming mullet (*Chelon labrosus*) sheds one vortex per half-stroke of its caudal fin upon reaching its maximum oscillatory displacement. Nauen and Lauder [19] have reported from their experimental investigations that chub mackerel (*Scomber japonicus*) sheds elliptical ring-shaped vortices in its wake with centered jet flows. Tytell [20] have argued that a bluegill sunfish (*Lepomis macrochirus*) produces and sheds flow structures like hairpin vortices through its caudal fin. In his study, vortices traversed from the median fins had not interaction with those produced by the tail. The numerical simulations of Borazjani and Sotiropoulos [16] have demonstrated that three-dimensional (3D) vortex structures (rings or hairpin-like) shed by a mackerel (*Scomber scombrus*) and its wake configurations, in terms of single- and double-row vortex streets, depend on Strouhal number. Borazjani and Daghooghi [17] have provided evidence for a leading-edge vortex attached with caudal fins of carangiform swimmers to increase thrust production. They have also shown that undulatory fish kinematics helps this vortex stabilize over the surface of the tail.

The role of median fins, e.g., anal and dorsal fins, in improving the propulsive performance of carangiform swimmers is another area of interest in bettering the design of autonomous underwater vehicles (AUVs). In this regard, Drucker and Lauder [21] have employed digital particle image velocimetry to reconstruct ringlike coherent flow structures produced and shed by pectoral fins of bluegill sunfish. Nauen and Lauder [22], Drucker and Lauder [23], and Standen and Lauder [24] have used the same technique to visualize flow characteristics around the fins of chub mackerel, rainbow trout (*Oncorhynchus mykiss*), and brook trout (*Salvelinus fontinalis*), respectively. Tytell *et al.* [25] have emphasized analyzing 3D flow features for swimming fish due to the presence of median fins on their posterior body regions by presenting their findings for kinematics and hydrodynamics of several carangiform swimmers, including brook trout, bluegill sunfish, and yellow perch (*Perca flavescens*). Liu *et al.* [26] analyzed the effect of median fins on the thrust production capability of Jack Fish (*Crevalle jack*). They have concluded that the leading-edge vortex (LEV) on the caudal fin, which is the primary contributor to thrust production, became stronger due to its interference with the vortices generated by the posterior body region. Zhong *et al.* [27] have designed a tuna-inspired robotic system to find that sharp dorsal fins would increase the hydrodynamic performance of the carangiform swimmer by reducing the angle of attack on the tail and assisting spanwise flow to greatly develop. Later, Han *et al.* [28] investigated the role of the shape and motion of dorsal and anal fins of sunfish on its hydrodynamic performance. When they enhanced the area of median fins with adjustments in the phase of their oscillatory motion, thrust and efficiency of the caudal fin were simultaneously improved by 25.6% and 29.2%, respectively. Recently, Wang *et al.* [29] have performed simulations for flows over finlets of yellowfin tuna (*Thunnus albacares*), which showed that these small pitching fins could reduce drag by 21.5% and power consumption by 20.8%. Similarly, Zhang *et al.* [30] have illustrated how two keel-like structures along the peduncle of tuna play a key role to improve its hydrodynamic characteristics.

There are various kinematic profiles of undulatory carangiform swimmers reported in the literature. For instance, Videler and Hess [31] have found the wavelength of kinematics of carangiform swimmers is equal to their body lengths. Jayne and Lauder [32] have shown that large mouth bass (*Micropterus salmoides*) swim with wavelengths 0.86 to 1.06 times their body lengths. Furthermore, mullet (*Chelon labrosus* Risso) have been observed to swim with wavelength equal to 1.11 times their body lengths [18]. Similar observations have been made by Donley and Dickson [14] for several carangiform swimmers. However, there remains a lack of knowledge regarding the role of wavelength of undulatory motion of fish in determining their thrust production capacity and power consumption, especially in relation to their real physiology. Addressing this knowledge gap becomes

more significant when determining the required flexibility at robotic joints to design and operate bio-inspired vehicles. Answering this important scientific question will also contribute greatly to our understanding of the biological evolution of fish, in which they have achieved such specific motion and flexibility for optimum swimming. Earlier, Borazjani and Sotiropoulos [33] performed numerical simulations to examine how the hydrodynamic performance of mackerel, which is a carangiform swimmer, and petromyzontiformes, an anguilliform swimmer, would be affected if their respective kinematic patterns were exchanged. However, their study was limited due to the absence of mackerels' median fins in their physiological models. Also,  $\lambda$  was restricted to only two values:  $\lambda = 0.642L$  and  $0.95L$ . Considering a foil as the representative cross section of a fish, Khalid *et al.* [34] have conducted numerical investigations to understand the effect of waveform on hydrodynamic performance parameters including thrust, power consumption, and efficiency. They have concluded that anguilliform swimmers outperform carangiform ones when they swim at  $\lambda > L$ . However, carangiform swimmers produce more thrust and efficiency for  $\lambda < L$ . These findings seem to imply that natural swimmers may choose their  $\lambda$  based on other biological needs and not to enhance their swimming performance. In this work, we further build on this by performing high-fidelity simulations for real Jack Fish with both original and prescribed kinematics. Here we explain why large wavelengths ( $\lambda^* = \lambda/L \geq 1$ ) suit hydrodynamics of Jack Fish representing carangiform swimmers.

Furthermore, we choose Jack Fish for our present study due to particular reasons that are outlined now. Some researchers have used other carangiform swimmers, such as tuna [29,30] and sunfish [28]. These species have some distinct morphological features that affect their hydrodynamics. For example, tuna has keel-like structures [30] and finlets [29] near its caudal fins, which significantly change its swimming performance. Furthermore, sunfish has median fins (dorsal and anal fins) with large aspect ratios [28] such that the effect of structural flexibility becomes more pronounced. Such constraints lead us to select Jack Fish for this study, which have less complexity in the wake.

## II. COMPUTATIONAL METHODOLOGY

### A. Physiological model and kinematics of Jack Fish

To reconstruct physiological structures of the trunk and median and caudal fins of Jack Fish and its kinematics, we employ the data recorded and reported previously by Liu *et al.* [26]. Although the procedure to capture the fish motion and its geometry along with the statistical details has been covered by Liu *et al.* [26], we present its important points here for completeness. The present model is of Crevalle Jack (*Caranx hippos*), which is classified as a carangiform swimmer. It is important to highlight that their body kinematics did not significantly change with the increasing swimming speed. The total height and width of this fish are  $0.286L$  and  $0.144L$ , respectively, where  $L$  is the total length of this fish. The area of the caudal fin is  $0.023L^2$ . The normalized height and length of the caudal fin are  $0.315L^2$  and  $0.244L^2$ , respectively.

In this study, we add median fins, the dorsal and anal fins, because these flexible membranous structures contribute towards the propulsive functionality of a fish. Its trunk is modeled as a solid body with a closed surface and the dorsal, anal, and caudal fins are membranes with zero thickness. Each surface is represented by triangular mesh, where the main body is composed of 11 358 nodes and 22 712 elements. The surface of the caudal fin has 1369 nodes and 2560 elements, while the dorsal and anal fins are composed of 885 and 895 nodes with 1664 and 1680 elements, respectively (see Fig. 1). The measured original wavelength from the midline profiles is approximately  $1.05L$ . The measured Strouhal number ( $St$ ) for these recordings remains at 0.30, where  $St = 2A_0 f / U_\infty$  with  $f$  being the excitation/flapping frequency of the caudal fin,  $A_0$  as the maximum one-sided oscillation amplitude of the caudal fin, a measure of the wake width, and  $U_\infty$  as the free-stream velocity.

In our present work, we perform 3D numerical simulations for flows over the complete physiological model of Jack Fish with its real and prescribed kinematics, based on which  $0.65 \leq \lambda \leq 1.25$ .

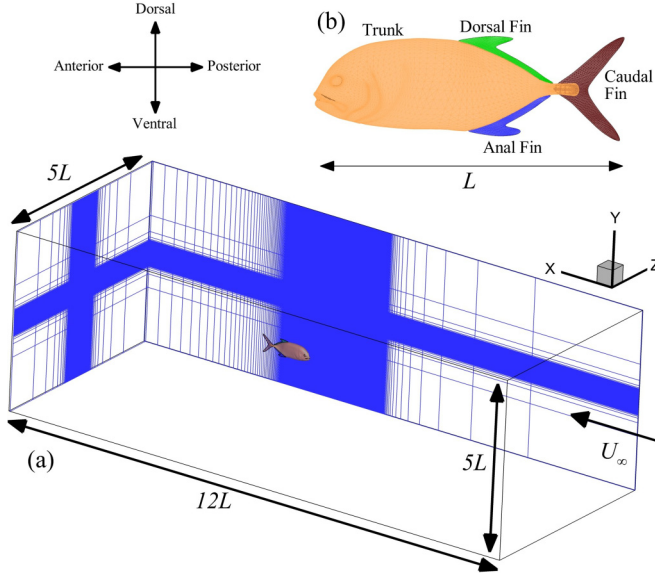


FIG. 1. (a) Virtual tunnel for simulating flows over Jack Fish with its dimensions and (b) the physiological model of Jack Fish covered with a mesh to indicate marker points to track their motion.

The carangiform amplitude profile is given by the following relation [34–36]:

$$A\left(\frac{x}{L}\right) = 0.02 - 0.0825\left(\frac{x}{L}\right) + 0.1625\left(\frac{x}{L}\right)^2, \quad 0 < \frac{x}{L} < 1, \quad (1)$$

where  $A(x/L)$  denotes the local amplitude at a given spatial position along the fish body, nondimensionalized by its total length ( $L$ ). Here the coefficients are calculated based on the data provided for a steadily swimming pollachius virens fish, which is a carangiform swimmer [37] with local amplitudes of  $A(0) = 0.02$ ,  $A(0.2) = 0.01$ , and  $A(1.0) = 0.10$ . The undulatory kinematics takes the following form in both cases:

$$z(x/L, t) = A(x/L) \sin[2\pi(x/\lambda - ft) + \phi]. \quad (2)$$

Here  $2\pi/\lambda$  defines the wave-number ( $k$ ) for the waveform of the kinematic profile along the swimmer's body and  $\phi$  denotes the phase of oscillation. In Fig. 2 we present the comparison of real and prescribed ( $\lambda^* = 1.05$ ) kinematics with  $\phi = -5.5^\circ$  for four different points on the trunk and anal, dorsal, and caudal fins. Here  $\tau$  represents the time-period for one complete undulation cycle. The points marked on the trunk and all three fins are not positioned on a vertical line. We select their locations over the most flexibly moving regions on the fins, which are also farthest from their respective bases attached to the main body of the fish. It is clear that Eq. (2) for the prescribed motion mimics the real kinematics very well.

Figure 3 exhibits the comparison of forms of Jack Fish with the real and prescribed motion at  $\lambda^* = 1.05$  for two instants in time. We notice that the dorsal and ventral sides of the caudal fin show asymmetry in their oscillation amplitudes, and it could happen due to the flexible membranous structure of the fish tail. Other than flexibility of the caudal fin, the possible presence of multiple wavelengths in small ranges along the body length of a real fish may be the cause for discrepancies in current results compared to experiments. Particularly, these small ranges of  $\lambda$  along the body length of a real fish at some time instants [12,31,32] in experimental settings can cause differences between computational results obtained through prescribed kinematic profiles and experimental

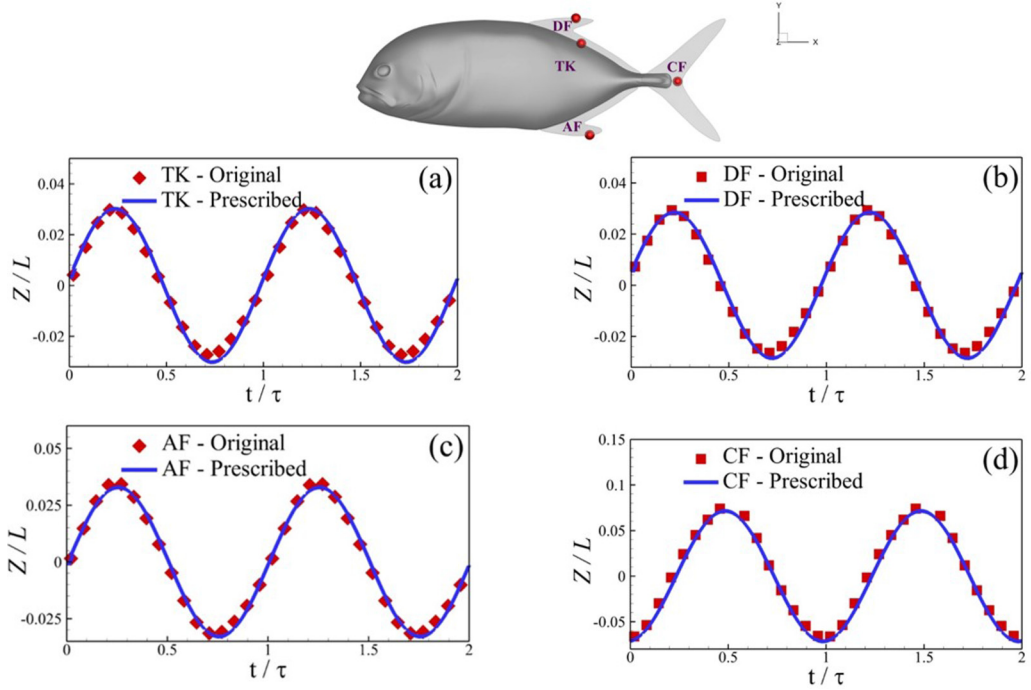


FIG. 2. Comparison of the real and prescribed kinematics ( $\lambda^* = 1.05$  and  $\phi = -5.5^\circ$ ) through temporal histories of displacements for four distinct points on the trunk and dorsal, anal, and caudal fins.

observations. Fish are known to use active kinematic strategies for subtle changes in coherent flow structures around them.

### B. Numerical solver

We perform 3D numerical simulations at  $Re = 3000$  and  $St = 0.33$ . Continuity and incompressible Navier-Stokes equations constitute the mathematical model for the fluid flow:

$$\frac{\partial u_j}{\partial x_j} = 0, \quad (3)$$

$$\frac{\partial u_i}{\partial t} + u_j \frac{\partial}{\partial x_j} (u_i) = -\frac{1}{\rho} \frac{\partial p}{\partial x_i} + \frac{1}{Re} \frac{\partial^2 u_i}{\partial x_j \partial x_j}, \quad (4)$$

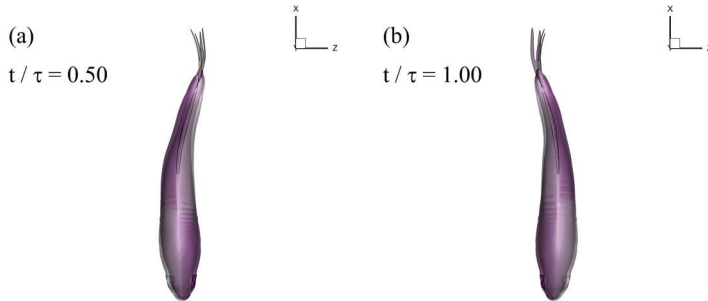


FIG. 3. Comparison of the real and prescribed ( $\lambda^* = 1.05$ ) motion of Jack Fish (with models in dark and light colors, respectively) at two time instants.

where indices  $i, j = 1, 2, 3$ ,  $x_i$  shows Cartesian directions,  $u_i$  denotes Cartesian components of the fluid velocity,  $p$  is the pressure, and  $Re = LU_\infty/\nu$  represents the Reynolds number with  $\nu$  denoting the kinematic viscosity of the fluid. We solve the described governing model for fluid flow using a Cartesian grid-based sharp-interface immersed boundary method, where the prescribed wavy kinematics is enforced as a boundary condition for the swimmers. We impose such conditions on immersed bodies through a ghost-cell procedure [26,28,29,38,39] that is suitable for both rigid and membranous body-structures.

We solve this governing mathematical model for fluid flows using a Cartesian grid-based sharp-interface immersed boundary method [38], where the spatial terms are discretized using a second-order central difference scheme and a fractional-step method for time marching. This makes our solutions second-order accurate in both time and space. We utilize Adams-Bashforth and implicit Crank-Nicolson schemes for numerical approximations of convective and diffusive terms, respectively. The prescribed wavy kinematics is enforced as a boundary condition for the swimmer's body. We prescribe these conditions on immersed bodies through a ghost-cell procedure [38], which works well for both rigid and membranous structures [26,28,40]. More details on this solver and its applicability to solve bio-inspired flow problems are available in the literature [26,28,29,39,40].

Next, we employ Dirichlet boundary conditions for flow velocities on all sides except the left boundary, where Neuman conditions are used at the outflow boundary (see Fig. 1). The slices on the back and left boundaries show the regions with high mesh density in order to adequately resolve the flow features around the structure and its wake. We use a mesh size of  $(N_x, N_y, N_z) = (385, 129, 161)$ , which yields a total of 7.99 million nodes. For the mesh sensitivity analysis, readers are referred to Liu *et al.* [26] and Khalid *et al.* [40].

The real advantage of using our advanced computational solver lies in its ability to handle large-amplitude oscillations of complex-shaped bodies and their interaction with surrounding fluids. Because numerous parameters cannot be controlled with real animals in laboratory conditions, our numerical solver gives us more freedom to prescribe different kinematic profiles over real fish-like anatomical models and examine their hydrodynamic performance. Such techniques are also very helpful in revealing how dynamics of coherent structures around these bodies alter temporal profiles of hydrodynamic forces [41–45].

### III. RESULTS AND DISCUSSION

In this section, we first present hydrodynamics performance parameters, thrust coefficient ( $C_T$ ), power consumption ( $C_P$ ), and swimming efficiency. The bar over a coefficient represents its respective cycle-averaged value. Next, we discuss the wake topology and vortex dynamics for variations in the wavelength of the prescribed motion of Jack Fish and its real kinematics.

Several previous studies [26,27,46] demonstrate that inertial effects remain dominated in flow dynamics around swimming animals at  $Re \gtrsim 10^3$ . Moreover, the primary coherent structures and their dynamics around different marine species bear close resemblance to experimental observations. These findings justify our choice of keeping  $Re = 3000$ , which is large enough for the formation of turbulent structures without the complexities of high- $Re$  3D turbulent flow complexities.

#### A. Hydrodynamic performance parameters

The hydrodynamic performance parameters are determined by projecting relevant fluid flow variables around the body to obtain surface pressure and shear stress. These quantities are further integrated to compute hydrodynamic forces and power consumed by the swimmer. The following relation defines the power expended by the fish:

$$P = \oint (\bar{\sigma} \cdot \mathbf{n}) \cdot \mathbf{V} ds, \quad (5)$$

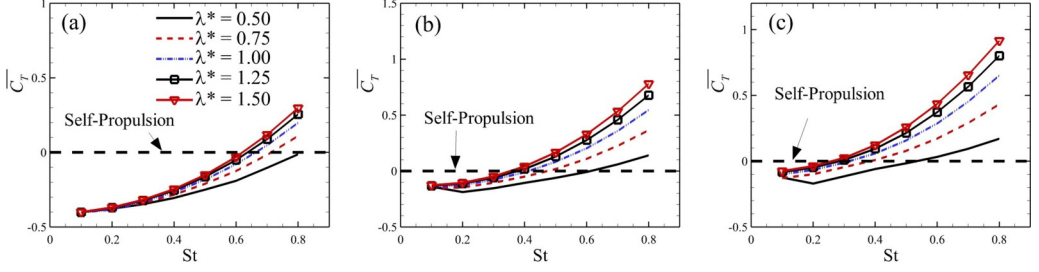


FIG. 4. Time-averaged thrust coefficient ( $\overline{C}_T$ ) for an undulating foil as the function of Strouhal number for (a)  $Re = 100$ , (b) 1000, and (c) 5000 [34].

where  $\oint$  is the surface integral operator,  $\overline{\sigma}$  denotes the stress tensor,  $\mathbf{n}$  represents the vector normal to the body surface, and  $\mathbf{V}$  represents the fluid velocity vector adjacent to the swimmer. We obtain the nondimensionalized coefficients of axial force, drag ( $F_D$ ) or thrust ( $F_T$ ), and power through

$$C_D = F_D / (0.5\rho U_\infty^2 A_s), \quad (6)$$

$$C_T = -C_D, \quad (7)$$

$$C_P = P / (0.5\rho U_\infty^3 A_s), \quad (8)$$

where  $A_s$  denotes the surface area of caudal fin of Jack Fish. Now, we define swimming efficiency or Froude's efficiency using

$$\eta = \overline{C}_T \tilde{U} / \overline{C}_P. \quad (9)$$

The case of  $St = 0.30$  is selected based on the real fish, which were found to swim at  $St \sim 0.30$ . Another motivation for choosing this parameter comes from our 2D numerical simulations for flows over an undulating foil undergoing carangiform undulations for a large set of kinematic and flow parameters [34]. We present variations of cycle-averaged thrust coefficients as functions of  $\lambda^*$  and  $St$  from Khalid *et al.* [34] in Fig. 4 at  $Re = 100$ , 1000, and 5000. These plots show that a lower undulatory wavelength would make the swimmer reach its steady swimming or self-propelling state ( $\overline{C}_T = 0$ ) at a higher  $St$ , which decreases with increasing  $Re$ . For a viscous flow regime ( $Re = 100$ ), the swimmer undergoes self-propulsion for  $St > 0.60$ . The swimmer starts swimming steadily at  $St \sim 0.40$  and  $0.30$  for  $Re = 1000$  and 5000, respectively. Hence, it provides another rationale behind the selected value of  $St$  in our present simulations.

The cycle-averaged values of thrust coefficient ( $\overline{C}_T$ ) for the caudal fin and drag coefficients ( $\overline{C}_D$ ) for the trunk and median fins are shown in Fig. 5 for Jack Fish with prescribed motion after solutions attain their steady states. These coefficients are normalized by their respective values provided in Table I for the real kinematics of this fish. It is interesting to note that the caudal fin of Jack Fish produces the largest thrust when it undulates with  $\lambda^* = 1.05$ . This value of  $\lambda^*$  seems to be an optimal condition, and the real fish also undulates with almost the same  $\lambda^*$ . As we increase  $\lambda^*$ , the drag

TABLE I. Cycle-averaged hydrodynamics performance parameters for the real Jack Fish kinematics.

Quantity	Caudal Fin (CF)	Trunk (TK)	Anal Fin (AF)	Dorsal Fin (DF)
$\overline{C}_{T_o}$	0.2316	–	–	–
$\overline{C}_{D_o}$	–	0.6373	0.0165	0.0127
$\overline{C}_{P_o}$	0.6202	0.6401	0.0487	0.046
$\eta_o$	0.1972	–0.5257	–0.1786	–0.1454

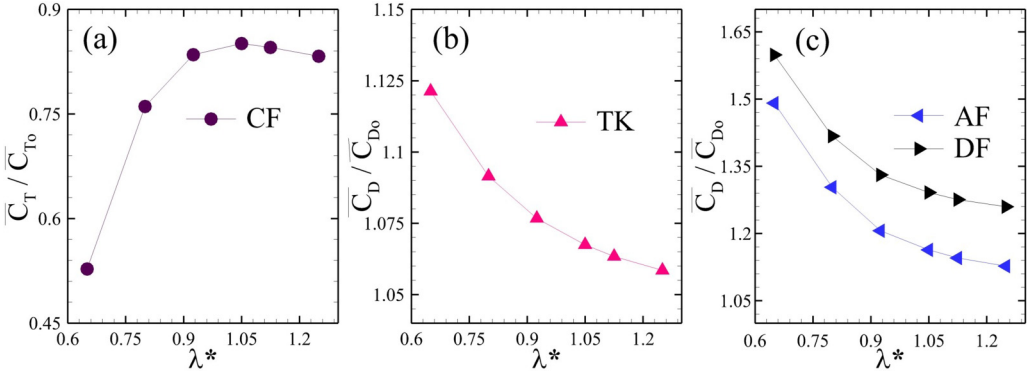


FIG. 5. (a) Thrust coefficient of the caudal fin, (b) drag coefficient of the trunk, and (c) drag coefficient of the anal and dorsal fins, where each cycle-averaged coefficient is normalized by its respective value for the real fish kinematics.

production by the trunk and median fins reduces. Thus, it can explain why real carangiform fish choose this  $\lambda^*$  in order to swim steadily.

Figure 6 shows  $\overline{C_P}$  that is normalized by  $\overline{C_{P_0}}$  for all cases with the defined kinematics, where  $\overline{C_{P_0}}$  is the respective power coefficient for each component of the Jack Fish. Greater wavelengths increase power consumption by all membranous fins. However, the trunk needs to consume reduced power when the fish swims with a larger  $\lambda^*$ . Most of the mechanical power is produced in precaudal regions of carangiform-type fish, which is further transferred to caudal fin through skin and skeleton [12]. We also observe that all cases with the prescribed motion show a lower  $\overline{C_P}$  than the real kinematics.

We also show the hydrodynamic efficiency ( $\eta$ ), normalized by  $\eta_0$ , of the caudal fin in Fig. 7(a). Our results indicate that the carangiform swimmer is more efficient when swimming with  $\lambda^* = 0.80$ . Increasing the wavelength would reduce its swimming efficiency. It is interesting that the real swimmer attains the least swimming efficiency compared to those with prescribed kinematics. It may be an artifact of how Froude's efficiency is mathematically defined. It may also be caused due to a lower Reynolds number considered for our present computational investigations. It is worth noting that Triantafyllou *et al.* [47] have identified that oscillating airfoils achieve better efficiency at a Strouhal range of 0.3–0.5, which coincides with the range of operating flapping in real natural swimmers.

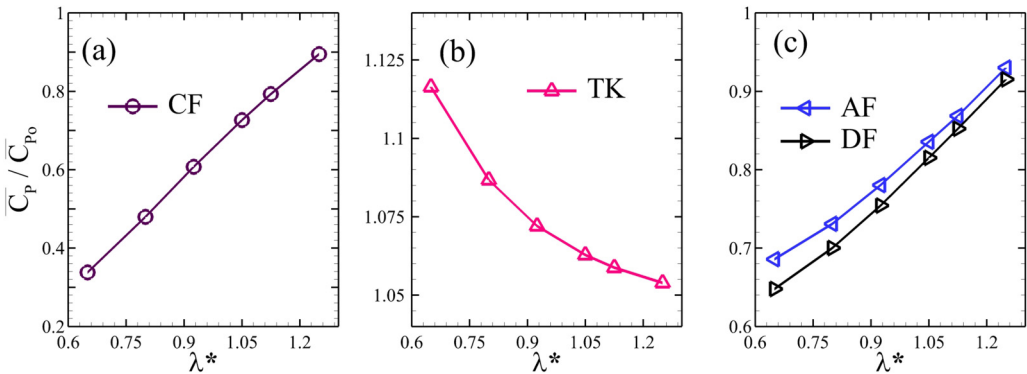


FIG. 6. Cycle-averaged power coefficient of (a) the caudal fin, (b) trunk, and (c) anal and dorsal fins, where each coefficient is normalized by its respective value for the real fish kinematics.



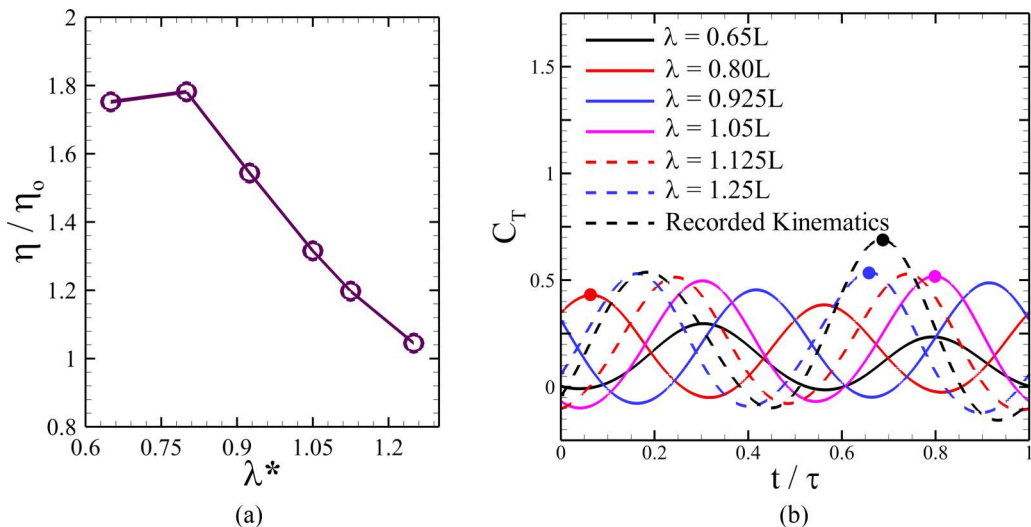


FIG. 7. (a) Hydrodynamic efficiency of the caudal fin of Jack Fish as a function of undulatory wavelength where  $\eta$  is normalized by its value for the real fish kinematics and (b) temporal histories of  $C_T$  of the caudal fin for the real and prescribed motion.

The real kinematics of Jack Fish surpasses the performance of those with the prescribed motion in all cases for thrust production of the caudal fin and drag production for the trunk and median fins. However, individual fins with the real kinematics motion consume more power to achieve the same hydrodynamic motion, while this is reversed for the trunk. Our analysis depicts that natural carangiform swimmers aim to produce more thrust from their caudal fins while minimizing their efforts to consume less power by their trunks. A wavelength larger than its body length helps it achieve this superior performance.

In Fig. 7(b) we show unsteady thrust of the caudal in one oscillation cycle for all cases. Because the wavelength controls both the oscillation amplitude and phase of the fish body, we see that the peak value of  $C_T$  occurs during the first half of the oscillation cycle for  $\lambda^* < 0.925$  and in the second half for greater values of  $\lambda^*$ . This requires a more detailed investigation combined with a discussion of the wake dynamics, which is presented in the next subsection. Moreover, we observe an asymmetry in the temporal profile of  $C_T$  produced by the originally recorded kinematics of the fish. It is caused by the asymmetric motion of the caudal fin on its ventral side during leftward and rightward strokes, as has also been previously explained by Liu *et al.* [26].

### B. Wake topology and vortex dynamics

It is important to deeply analyze and understand the topology and dynamics of 3D coherent structures around the carangiform swimmer and in its wake because these structures and their interactions play a primary role to determine its hydrodynamic performance. Now, in order to extract these vortices, we employ the  $Q$ -criterion. First, we focus on the overall wake configurations produced by the swimmer's undulatory motion with different  $\lambda^*$ . Figure 8 presents these flow characteristics from the top view. It is clear that several large- and small-scale vortices are generated and shed in the wake by the fish. For  $\lambda^* = 0.80$ , it is clear in Fig. 8(a) that the vortices do not have elongated arms along the streamwise direction, i.e., the  $x$ -axis, and their laterally oriented legs along the  $z$ -axis are more visible. However, as the fish increases its  $\lambda^*$ , we observe the formation of long streamwise arms of vortices in the wake. This characteristic justifies the increase in thrust generation [48] at larger  $\lambda^*$ . Another important feature in these visualizations is the presence of green-colored

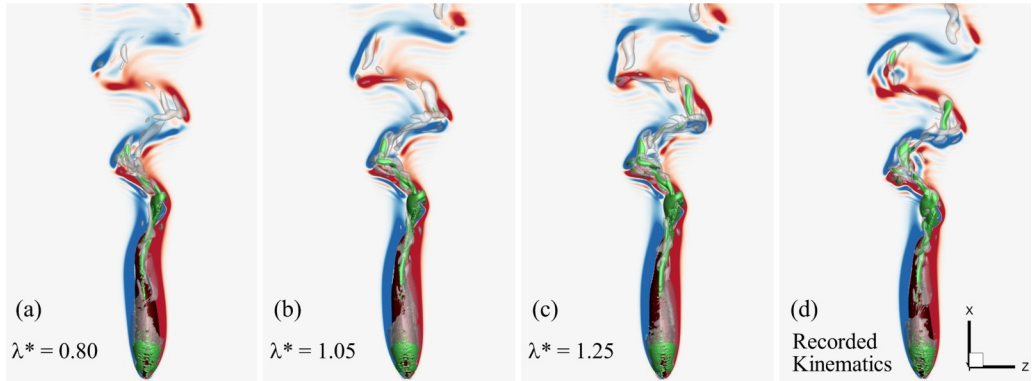


FIG. 8. Top views of 3D vortex structures around Jack Fish undulating with  $\lambda^* =$  (a) 0.80, (b) 1.05, (c) 1.25, and (d) real kinematics where the coherent structures are identified by the isosurface of the  $Q$ -criterion. The isosurface  $Q = 5$  is in gray and  $Q = 30$  is in green. Two-dimensional blue and red vortices, with negative and positive vorticity, respectively, are also shown on the midplane of these flow fields.

vortex cores (with a greater  $Q$  value) farther in the wake for greater  $\lambda^*$ . It shows the capability of the fish to produce a stronger wake under such kinematic conditions.

Next, Fig. 9 provides a detailed overview of vortices produced by different fins of Jack Fish during its caudal fin's rightward stroke with its originally recorded kinematics. We define their nomenclature for our further analyses. Because there are various 3D vortices around Jack Fish, it is important to sequentially name them and track them to see their effects on the hydrodynamics of this swimmer. We observe a vortex identified in Fig. 9 as DFV (dorsal fin vortex) developing on the dorsal fin. We also notice another vortex, named AFV (anal fin vortex), on the anal fin. Simultaneously, there develops a vortex around the posterior extension of the dorsal fin and is

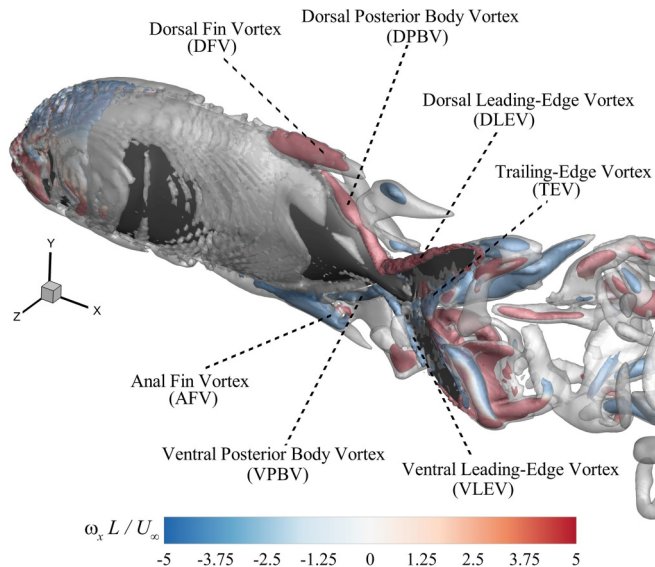


FIG. 9. Vortex topology around Jack Fish for originally recorded kinematics, where coherent structures are colored by the isosurface of the  $Q$ -criterion. The isosurface  $Q = 5$  is in light-gray color, whereas inner vortex cores with  $Q = 30$  are colored by the nondimensional  $x$ -component of vorticity ( $\omega_x$ ).

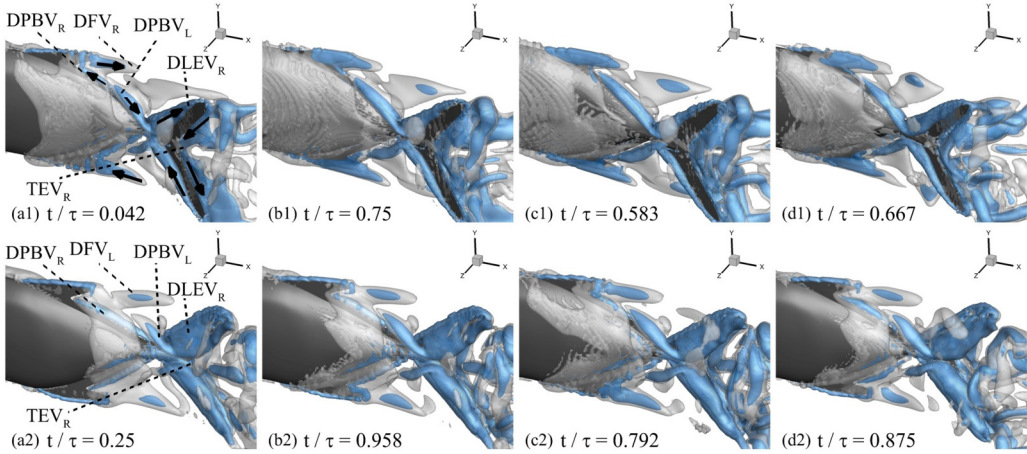


FIG. 10. Vortex dynamics in the vicinity of the caudal fin of Jack Fish undulating with the prescribed motion at  $\lambda^* = 0.80, 1.05, 1.25$ , and the real kinematics in the first, second, third, and fourth columns, respectively, and the top and bottom rows show flow states at their respective beginning of rightwards stroke and in its middle stage, respectively. Here wake structures are colored by the isosurface of the  $Q$ -criterion. The isosurface  $Q = 5$  is in gray and  $Q = 30$  is in blue. The latter highlights the vortex core.

denoted as DPBV (dorsal posterior body vortex). Another vortex is formed on the posterior side of the anal fin. It is important to mention that the vortices around the anal fin (AFV and VPBV) have  $\omega_x$  in the opposite direction to those (DFV and DPBV) on the dorsal fin as indicated by colors of the contours. At this time instant, a weakening DFV (with blue-colored core indicating its negative  $\omega_x$ ) produced during the previous half-stroke is seen to approach the caudal fin on its dorsal side. Furthermore, we also find the attachment of vortex tubes on the leading edge of the caudal fin. On its dorsal side, the vortex tube, labeled as DLEV (dorsal leading-edge vortex), has positive  $\omega_x$ , whereas the vortex tube VLEV (ventral leading-edge vortex) on the ventral side has negative  $\omega_x$ . Borazjani and Daghooghi [17] have concluded that this LEV becomes the primary factor for thrust production by the tail of a carangiform swimmer. Its trailing edge is wrapped by another vortex tube, identified as TEV in Fig. 9. It is important to mention that orientations of vorticity components elucidate the formation of 3D vortices of distinct geometries, such as rings and hairpins etc.

Figure 10 illustrates the vortex dynamics around the fins of Jack Fish for its real kinematics and prescribed motion with  $\lambda^* = 0.80, 1.05, 1.25$ . Here subscripts “L” and “R” represent the vortices produced during the leftward and rightward oscillations, respectively. In each half oscillation cycle, DFV, AFV, and PBVs are formed and traverse downstream. These small vortices are bound to be intercepted by the caudal fin. The timing of these phenomena impacts the swimmer’s hydrodynamic performance significantly and capturing of vortices by the caudal fin enhances the strength of LEVs formed around the caudal fin [26,49].

The first and second rows in Fig. 10 show vortex configurations when the caudal fin begins its rightward stroke and is in the middle of it, respectively. Time instants in these plots are different for different  $\lambda^*$  because the undulatory wavelength affects both amplitude and phase of the wavy motion. In Fig. 10(a1), black-colored arrows show the orientations of the 3D coherent structures using the directional sense of the Cartesian components of vorticity vector. In each plot in the first row of Fig. 10, vortex tubes, denoted by DLEV<sub>R</sub>, VLEV<sub>R</sub>, and TEV<sub>R</sub>, form a ring-shaped vortex structure that is clarified by directions of arrows around the caudal fin. Similar observations have been reported earlier by Liu *et al.* [26] and Khalid *et al.* [40] for Jack Fish, and Han *et al.* [28] for sunfish. As the caudal fin progresses for its rightward stroke, the two vortex cores DLEV<sub>R</sub> and VLEV<sub>R</sub> grow to span over its left side (see plots in the bottom row of Fig. 10). This process also involves interference of DPBV<sub>R</sub> with DLEV<sub>R</sub> and VPBV<sub>R</sub> with VLEV<sub>R</sub>. Due to the same

directional sense of vorticity vectors of these two vortex pairs (DPBV<sub>R</sub> and DLEV<sub>R</sub> and VPBV<sub>R</sub> and VLEV<sub>R</sub>), there occurs constructive interference [50,51] between them. This phenomenon further enhances the circulation and strength of LEVs before their merger with the TEV. However, the previously shed DFV<sub>L</sub> and AFV<sub>L</sub> undergo destructive interference with DLEV<sub>R</sub> and VLEV<sub>R</sub>, respectively. This interference mechanism is related to the merger of vortices with oppositely signed vorticity [50,51], which results in degradation of their strength and circulation. Furthermore, we find that DFV loses its strength in terms of the reduced size of its posterior end for larger  $\lambda^*$  in Figs. 10(b1), 10(c1), and 10(d1). In fact, the originally recorded kinematics of Jack Fish produces the weakest DFV.

It is important to describe that we do not observe distinct ring-shaped or hairpin-like coherent structures as observed by Borazjani and Sotiropoulos [16] at  $Re = 300$  and  $4000$  with  $St = 0.20$  and  $0.30$ , respectively. They have argued that the formation of a single-row or double-row wake is dependent on Strouhal number. Liu *et al.* [26] have also reported the shedding of two ringlike coherent structures in the wake in each undulation cycle of Jack Fish. They have also found the presence of a double-row vortex wake for  $St > 0.30$ . In our present flow and kinematic conditions, the vortex-ring structures formed around the caudal fin depicts double-row vortex streets in the wake as also claimed by Liu *et al.* [26] and Han *et al.* [28] for different carangiform swimmers. Nonetheless, our simulations demonstrate transitions from single-row wake configurations to double-row wake structures behind the carangiform swimmer (see Fig. 8). It corroborates with the observation of Borazjani and Sotiropoulos [16], where the wake completely exhibits coherent structures arranged neither in a single row nor in a double row.

To further analyze the interaction between different vortices, we focus on sectional views of flow fields in the vicinity of Jack Fish. First, we plot contours of  $\omega_x$  nondimensionalized by  $L$  and  $U_\infty$  on the vertical plane passing through 90% of the body length in Fig. 11 at three different time instants for different kinematic conditions. Figure 11(a1) explains the positioning of distinct vortices produced during rightward and leftward strokes of the caudal fin. A careful look at the plots in the first row of Fig. 11 reveals that as we increase  $\lambda^*$ , the fish is able to keep DFV<sub>L</sub> away from the caudal fin. It implies that the fish attempts to reduce the level of destructive interference between DFV<sub>L</sub> and LEV<sub>R</sub>. These contour plots also exhibit the presence of LEV<sub>L</sub> attached on the right side of the caudal fin. For the real kinematics and  $\lambda^* = 1.05$  and  $1.25$ , we notice its grown size highlighting its greater strength under such conditions. This persisted attachment of LEV<sub>L</sub> increases the pressure difference between the two sides of the caudal fin to greatly enhance its thrust production. We also notice from the visibility of two vortex cores near the root of the caudal fin that TEV and LEV<sub>L</sub> are distinct for larger  $\lambda^*$ s. Evidently, the strengths of LEV<sub>R</sub> and TEV are the greatest for the case with real kinematics. In the later stages of the rightward stroke of the caudal fin (see contour plots in the middle and bottom rows of Fig. 11), LEV<sub>R</sub> grows owing to its constructive interference with DPBV<sub>L</sub>, and LEV<sub>L</sub> vanishes due to its complete shedding in the wake. Simultaneously, a larger  $\lambda^*$  helps the caudal fin to keep DFV<sub>L</sub> away from itself, which is likely to reduce the strength of LEV<sub>R</sub>. Liu *et al.* [26] have reported  $\lambda^* \approx 1.05$  of Jack Fish for its recorded kinematics. One possible reason for superior hydrodynamic performance of Jack Fish here is the flexibility of its caudal fin. This structural flexibility helps the fish maintain a dorso-ventral asymmetry during its undulation. This asymmetric pattern was also mentioned by Liu *et al.* [26]. It is worth mentioning that physical mechanisms elaborated in this study are very different from those presented by Liu *et al.* [26] provide more insights about the role of median fins to improve the hydrodynamic performance of the caudal fin of Jack Fish.

To better explain the dynamics of LEV<sub>R</sub>, we also compute its circulation ( $\Gamma$ ) during the rightward stroke of the caudal fin. For this quantification, we utilize our methodology presented earlier in Ref. [34]. Circulation is a measure of the strength of a vortex and is mathematically defined as the line integral of the velocity field over its boundary ( $\Gamma = \oint \mathbf{V} \cdot d\mathbf{l}$ ) or the surface integral of the vorticity field over the area of this vortex ( $\Gamma = \iint_S \omega \cdot d\mathbf{s}$ ). We have developed a technique to avoid an overlap with a vortex boundary with another one present in its vicinity [52]. Readers are referred to Ref. [34] for more details about this method. Because the caudal fin physically performs

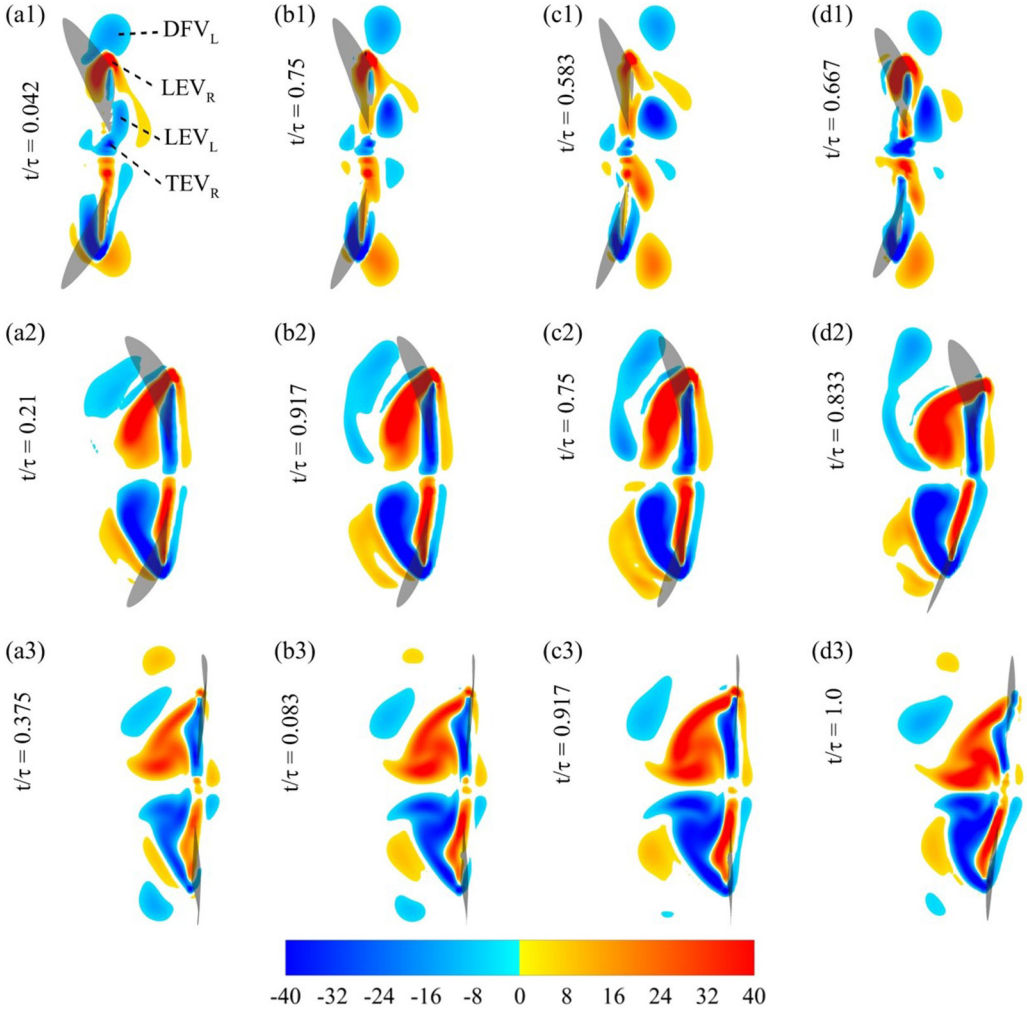


FIG. 11. Vortex dynamics with contours of  $\omega_x^* = \omega_x L / U_\infty$  in a vertical plane located at  $0.90L$  on the caudal fin of Jack Fish undulating with the prescribed motion at  $\lambda^* = 0.80, 1.05, 1.25$ , and the real kinematics in the first, second, third, and fourth columns, respectively.

its rightward strokes during different instants of its time periods for different  $\lambda^*$ , Figure 12(a) plots  $\Gamma_x$ , nondimensionalized by  $L$  and  $U_\infty$ , as a function of a hypothetical timescale  $t^*$  in order to make a precise comparison of the strength of vortices. Here  $t^*$  brings the caudal fin passing through the same stages of its rightward stroke with different  $\lambda^*$ . Jack Fish undulating with larger  $\lambda^*$  produces stronger LEVs. In the beginning of this half-stroke, LEV gains strength and starts losing it during the middle stage. Jack fish with real kinematics is able to have the strongest LEV with the greatest circulation levels, most probably due to the flexible motion of its tail and/or slight variations in its wavelength through its muscles activation. It is interesting to point out that the prescribed kinematics with  $\lambda^* = 1.05$  produces more circulation compared to that with  $\lambda^* = 1.25$  during the first quarter of the rightward stroke. However, the higher undulatory wavelength adds more strength to the LEV in later stages. Based on these observations, it appears that Jack Fish makes adjustments in the motion of its caudal fin during the earlier stages of its caudal fin's strokes to actively control the flow around it. This fish behavior could not be captured by the prescribed kinematics.

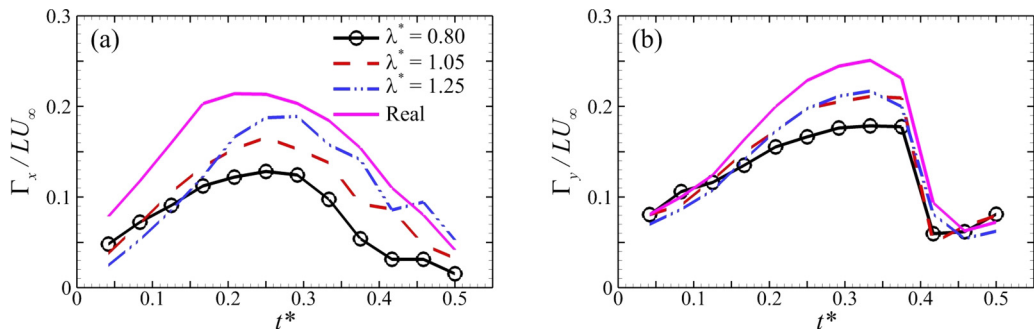


FIG. 12. Circulation of LEVs that remain attached with the caudal fin throughout its rightward flapping stroke.

Next, we qualitatively examine  $\omega_y$  of vortices around the caudal fin by extracting a slice near its dorsal end shown in Fig. 13 at the same time instants as used in Fig. 11. The contours show elevated strength of LEV for larger  $\lambda^*$ . Contour plots of  $\omega_y$  in the middle row of Figs. 13(a2), 13(b2), 13(c2), and 13(d2) also show that interaction of vortices produced on the posterior regions of the body not only helps  $LEV_R$  grow but also assists in developing its elongated part in the wake. At this stage, posterior parts of LEVs are detached from their main cores, which remain attached to the leading edge of the caudal fin. It appears that when  $LEV_R$  spans over the left side of the caudal fin, shown in Figs. 10(a2), 10(b2), 10(c2), and 10(d2), it initiates its detachment from the surface of the tail. This phenomenon is more pronounced for the real kinematics of Jack Fish in Fig. 13(d2). A possible contributing factor for this flow characteristic is the phase angle between the peduncle region and the caudal fin at the time of interaction between  $DPBV_L$  and  $DLEV_R$ . Akhtar *et al.* [49] have elaborated the role of phase angles between the kinematics of median and caudal fins of a carangiform swimmer. They have argued that this phase affects the angle of attack for the tail and subsequently affects its hydrodynamic performance to a great extent. Furthermore, Han *et al.* [28] have identified that variations in the phase of the flapping motion of median fins impacts the timing of posterior body vortices interacting with the LEV around the caudal fin. A leading phase angle for median fins enhances the efficiency of the caudal fin, whereas lagging phase angles help the swimmer produce higher thrust.

To further quantify the strength of LEVs, we compute their circulation ( $\Gamma_y$ ) using contours of  $\omega_y$  during rightward flapping strokes and plot in Fig. 12(b). We observe that larger wavelengths produce LEVs with greater circulation. From the cases with prescribed motion, we also find the  $LEV_L$  not gaining more strength when  $\lambda^*$  is increased beyond 1.05. Possibly owing to the flexibility of the caudal fin [26], the LEV is strongest for Jack Fish with the real kinematics. It is consistent with recent reports where flexible structures could produce higher thrust as compared to their rigid counterparts [7].

#### IV. CONCLUSIONS

In this work, we focus on the question of why Jack Fish, a carangiform swimmer, adopts an undulatory wavelength larger than its body length while swimming steadily. For this purpose, we reconstruct its physiological model and kinematics using high-speed imaging techniques. It is further utilized to prescribe its carangiform fish-like kinematics on the fish model and perform high-fidelity simulations for a range of undulatory wavelengths. Our findings show that  $\lambda^* = 1.05$  gives the following advantages to the swimmer: (1) caudal fin produces maximum thrust, (2) trunk experiences lesser drag under this kinematic condition compared to shorter  $\lambda^*$ , and (3) trunk expends lower power for its swimming with longer  $\lambda^*$ . Our 3D flow analyses demonstrate that the swimmer is able to produce and shed stronger coherent structures in its wake for  $\lambda^* > 1$ . We also notice that the

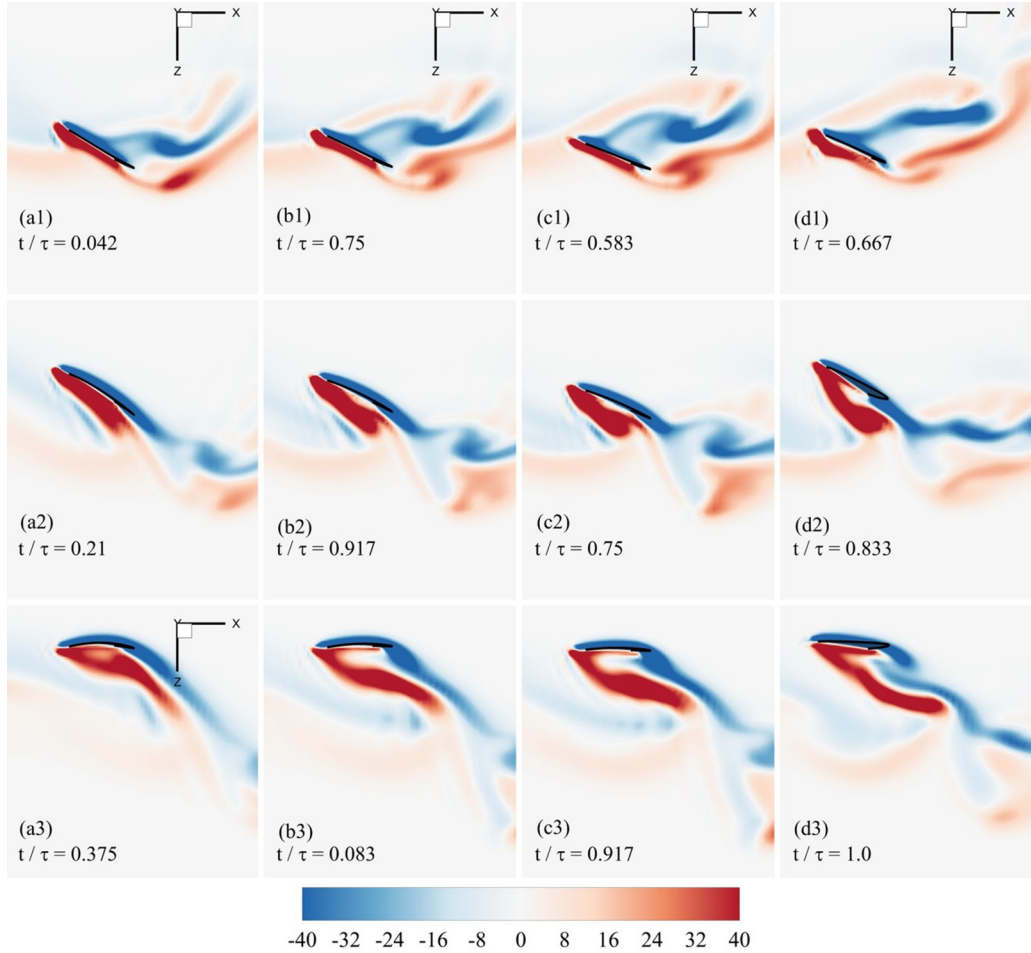


FIG. 13. Vortex dynamics with contours of  $\omega_y^* = \omega_y L / U_\infty$  in a lateral plane located on the dorsal side of Jack Fish undulating with the prescribed motion at  $\lambda^* = 0.80, 1.05, 1.25$ , and the real kinematics in the first, second, third, and fourth columns, respectively.

fish with its real kinematics outperforms others possibly due to its flexible caudal fin or utilization of muscle actuation for having multiple wavelengths for the undulating motion along its body. These subtle techniques may help the swimmer keep LEVs attached to their caudal fins and elongate their posterior legs in the wake. Jack Fish may also be able to avoid the destructive interactions of PBVs and LEVs around its caudal fin.

#### ACKNOWLEDGMENTS

M.S.U.K. is International Exchange Postdoctoral Research Fellow sponsored by China National Science Postdoc Foundation and Peking University. H.D. acknowledges the support from NSF CNS Grant No. CPS-1931929 and SEAS Research Innovation Awards of the University of Virginia.

[1] F. E. Fish, Advantages of aquatic animals as models for bio-inspired drones over present AUV technology, *Bioinspir. Biomim.* **15**, 025001 (2020).

- [2] J. Zhu, C. White, D. K. Wainwright, V. D. Santo, G. V. Lauder, and H. Bart-Smith, Tuna robotics: A high-frequency experimental platform exploring the performance space of swimming fishes, *Sci. Robot.*, **4**, 4615 (2019).
- [3] K. N. Lucas, G. V. Lauder, and E. D. Tytell, Airfoil-like mechanics generate thrust on the anterior body of swimming fishes, *Proc. Natl. Acad. Sci. USA* **117**, 10585 (2020).
- [4] R. Li, Q. Xiao, Y. Liu, L. Li, and H. Liu, Computational investigation on a self-propelled pufferfish driven by multiple fins, *Ocean Eng.* **197**, 106908 (2020).
- [5] Z. Wolf, A. Jusufi, D. Vogt, and G. V. Lauder, Fish-like aquatic propulsion studied using a pneumatically-actuated soft-robotic model, *Bioinspir. Biomim.* **15**, 046008 (2020).
- [6] F. C. J. Berlinger, M. Saadat, H. Haj-Hariri, G. V. Lauder, and R. Nagpal, Fish-like three-dimensional swimming with an autonomous, multi-fin, and biomimetic robot, *Bioinspir. Biomim.* **16**, 026018 (2021).
- [7] C. White, G. V. Lauder, and H. Bart-Smith, Tunabot flex: a tuna-inspired robot with body flexibility improves high-performance swimming, *Bioinspir. Biomim.* **16**, 026019 (2021).
- [8] D. K. Wainwright and G. V. Lauder, Tunas as a high-performance fish platform for inspiring the next generation of autonomous underwater vehicles, *Bioinspir. Biomim.* **15**, 035007 (2020).
- [9] Y. Luo, Q. Xiao, G. Shi, G. Pan, and D. Chen, The effect of variable stiffness of tuna-like fish body and fin on swimming performance, *Bioinspir. Biomim.* **16**, 016003 (2020).
- [10] M. Sfakiotakis, D. M. Lane, and J. B. C. Davies, Review of fish swimming modes for aquatic locomotion, *IEEE J. Oceanic Eng.* **24**, 237 (1999).
- [11] G. V. Lauder and P. G. A. Madden, Learning from fish: Kinematics and experimental hydrodynamics for robotics, *Int. J. Automat. and Comput.* **3**, 325 (2006).
- [12] J. Long, M. McHenry, and N. Boetticher, Undulatory swimming: How traveling waves are produced and modulated in sunfish (*Lepomis gibbosus*), *J. Exp. Biol.* **192**, 129 (1994).
- [13] A. C. Gibb, K. A. Dickson, and G. V. Lauder, Tail kinematics of the chub mackerel *Scomber japonicus*: Testing the homocercal tail model of fish propulsion, *J. Exp. Biol.* **202**, 2433 (1999).
- [14] J. M. Donley and K. A. Dickson, Swimming kinematics of juvenile kawakawa tuna (*Euthynnus affinis*) and chub mackerel (*Scomber japonicus*), *J. Exp. Biol.* **203**, 3103 (2000).
- [15] Q. Zhu, M. Wolfgang, D. Yue, and M. Triantafyllou, Three-dimensional flow structures and vorticity control in fish-like swimming, *J. Fluid Mech.* **468**, 1 (2002).
- [16] I. Borazjani and F. Sotiropoulos, Numerical investigation of the hydrodynamics of carangiform swimming in the transitional and inertial flow regimes, *J. Exp. Biol.* **211**, 1541 (2008).
- [17] I. Borazjani and M. Daghooghi, The fish tail motion forms an attached leading edge vortex, *Proc. R. Soc. London B* **280**, 2012207 (2013).
- [18] U. Müller, B. Van Den Heuvel, E. Stamhuis, and J. Videler, Fish foot prints: morphology and energetics of the wake behind a continuously swimming mullet (*Chelon labrosus Risso*), *J. Exp. Biol.* **200**, 2893 (1997).
- [19] J. C. Nauen and G. V. Lauder, Hydrodynamics of caudal fin locomotion by chub mackerel, *Scomber japonicus* (Scombridae), *J. Exp. Biol.* **205**, 1709 (2002).
- [20] E. D. Tytell, Median fin function in bluegill sunfish *Lepomis macrochirus*: Streamwise vortex structure during steady swimming, *J. Exp. Biol.* **209**, 1516 (2006).
- [21] E. G. Drucker and G. V. Lauder, Locomotor forces on a swimming fish: Three-dimensional vortex wake dynamics quantified using digital particle image velocimetry, *J. Exp. Biol.* **202**, 2393 (1999).
- [22] J. C. Nauen and G. V. Lauder, Locomotion in scombrid fishes: Visualization of flow around the caudal peduncle and finlets of the chub mackerel *Scomber japonicus*, *J. Exp. Biol.* **204**, 2251 (2001).
- [23] E. G. Drucker and G. V. Lauder, Locomotor function of the dorsal fin in rainbow trout: Kinematic patterns and hydrodynamic forces, *J. Exp. Biol.* **208**, 4479 (2005).
- [24] E. Standen and G. V. Lauder, Hydrodynamic function of dorsal and anal fins in brook trout (*Salvelinus fontinalis*), *J. Exp. Biol.* **210**, 325 (2007).
- [25] E. D. Tytell, E. M. Standen, and G. V. Lauder, Escaping flatland: three-dimensional kinematics and hydrodynamics of median fins in fishes, *J. Exp. Biol.* **211**, 187 (2008).



- [26] G. Liu, Y. Ren, H. Dong, O. Akanyati, J. C. Liao, and G. V. Lauder, Computational analysis of vortex dynamics and performance enhancement due to body-fin and fin-fin interactions in fish-like locomotion, *J. Fluid Mech.* **829**, 65 (2017).
- [27] Q. Zhong, H. Dong, and D. B. Quinn, How dorsal fin sharpness affects swimming speed and economy, *J. Fluid Mech.* **878**, 370 (2019).
- [28] P. Han, G. V. Lauder, and H. Dong, Hydrodynamics of median-fin interactions in fish-like locomotion: Effects of fin shape and movement, *Phys. Fluids* **32**, 011902 (2020).
- [29] J. Wang, Y. Ren, C. Li, and H. Dong, Tuna locomotion: A computational hydrodynamic analysis of finlet function, *J. R. Soc., Interface* **17**, 20190590 (2020).
- [30] J.-D. Zhang, H. J. Sung, and W.-X. Huang, Specialization of tuna: A numerical study on the function of caudal keels, *Phys. Fluids* **32**, 111902 (2020).
- [31] J. Videler and F. Hess, Fast continuous swimming of two pelagic predators, saithe (*Pollachius virens*) and mackerel (*Scomber scombrus*): A kinematic analysis, *J. Exp. Biol.* **109**, 209 (1984).
- [32] B. C. Jayne and G. V. Lauder, Speed effects on midline kinematics during steady undulatory swimming of largemouth bass, *Micropterus salmoides*, *J. Exp. Biol.* **198**, 585 (1995).
- [33] I. Borazjani and F. Sotiropoulos, On the role of form and kinematics of on the hydrodynamics of self-propelled body/caudal fin swimming, *J. Exp. Biol.* **213**, 89 (2010).
- [34] M. S. U. Khalid, J. Wang, H. Dong, and M. Liu, Flow transitions and mapping for undulating swimmers, *Phys. Rev. Fluids* **5**, 063104 (2020).
- [35] M. S. U. Khalid, I. Akhtar, and H. Dong, Hydrodynamics of a tandem fish school with asynchronous undulation of individuals, *J. Fluids Struct.* **66**, 19 (2016).
- [36] M. S. U. Khalid, I. Akhtar, H. Imtiaz, H. Dong, and B. Wu, On the hydrodynamics and nonlinear interaction between fish in tandem configuration, *Ocean Eng.* **157**, 108 (2018).
- [37] J. J. Videler, *Fish Swimming* (Chapman and Hall, London, 1993).
- [38] R. Mittal, H. Dong, M. Bozkurtas, F. Najjar, A. Vargas, and A. Von Loebbecke, A versatile sharp interface immersed boundary method for incompressible flows with complex boundaries, *J. Comput. Phys.* **227**, 4825 (2008).
- [39] J. Wang, Y. Ren, C. Li, and H. Dong, Computational investigation of wing-body interaction and its lift enhancement effect in hummingbird forward flight, *Bioinspir. Biomim.* **14**, 046010 (2019).
- [40] M. S. U. Khalid, J. Wang, I. Akhtar, H. Dong, and M. B. Liu, Modal decompositions of the kinematics of crevalle jack and the fluid-caudal fin interaction, *Bioinspir. Biomim.* **16**, 016018 (2021).
- [41] Z. Xiong and X. Liu, Numerical investigation on evolutionary characteristics of the leading-edge vortex induced by flapping caudal fin, *Phys. Fluids* **31**, 125117 (2019).
- [42] X. Bi and Q. Zhu, Fluid-structure investigation of a squid-inspired swimmer, *Phys. Fluids* **31**, 101901 (2019).
- [43] Y. Luo, Q. Xiao, Q. Zhu, and G. Pan, Pulsed-jet propulsion of a squid-inspired swimmer at high Reynolds number, *Phys. Fluids* **32**, 111901 (2020).
- [44] W. Wang, H. Huang, and X.-Y. Lu, Optimal chordwise stiffness distribution for self-propelled heaving flexible plates, *Phys. Fluids* **32**, 111905 (2020).
- [45] A. Khosronejad, L. Mendelson, A. H. Techet, S. Kang, D. Angelidis, and F. Sotiropoulos, Water exit dynamics of jumping archer fish: Integrating two-phase flow large-eddy simulation with experimental measurements, *Phys. Fluids* **32**, 011904 (2020).
- [46] I. Borazjani and F. Sotiropoulos, Numerical investigation of the hydrodynamics of anguilliform swimming in the transitional and inertial flow regimes, *J. Exp. Biol.* **212**, 576 (2009).
- [47] G. S. Triantafyllou, M. Triantafyllou, and M. Grosenbaugh, Optimal thrust development in oscillating foils with application to fish propulsion, *J. Fluids Struct.* **7**, 205 (1993).
- [48] M. S. U. Khalid, J. Wang, I. Akhtar, H. Dong, M. Liu, and A. Hemmati, Why do anguilliform swimmers perform undulation with wavelengths shorter than their bodylengths? *Phys. Fluids* **33**, 031911 (2021).
- [49] I. Akhtar, R. Mittal, G. V. Lauder, and E. Drucker, Hydrodynamics of a biologically inspired tandem flapping foil configuration, *Theor. Comput. Fluid Dyn.* **21**, 155 (2007).
- [50] R. Gopalkrishnan, M. S. Triantafyllou, G. S. Triantafyllou, and D. Barrett, Active vorticity control in a shear flow using a flapping foil, *J. Fluid Mech.* **274**, 1 (1994).

- [51] S. Kim, W.-X. Huang, and H. J. Sung, Constructive and destructive interaction modes between two tandem flexible flags in viscous flow, *J. Fluid Mech.* **661**, 511 (2010).
- [52] R. Godoy-Diana, C. Marais, J.-L. Aider, and J. E. Wesfried, A model for the symmetry breaking of the reverse Bénard-von Kármán vortex street produced by a flapping foil, *J. Fluid Mech.* **622**, 23 (2009).